

DF-Calib: Targetless LiDAR-Camera Calibration via Depth Flow

Shu Han Xubo Zhu Ji Wu Ximeng Cai Wen Yang Huai Yu Gui-Song Xia

Abstract—Precise LiDAR-camera calibration is crucial for integrating these two sensors into robotic systems to achieve robust perception. In applications like autonomous driving, on-line targetless calibration enables a prompt sensor misalignment correction from mechanical vibrations without extra targets. However, existing methods exhibit limitations in effectively extracting consistent features from LiDAR and camera data and fail to prioritize salient regions, compromising cross-modal alignment robustness. To address these issues, we propose DF-Calib, a LiDAR-camera calibration method that reformulates calibration as an intra-modality depth flow estimation problem. DF-Calib estimates a dense depth map from the camera image and completes the sparse LiDAR projected depth map, using a shared feature encoder to extract consistent depth-to-depth features, effectively bridging the 2D-3D cross-modal gap. Additionally, we introduce a reliability map to prioritize valid pixels and propose a perceptually weighted sparse flow loss to enhance depth flow estimation. Experimental results across multiple datasets validate DF-Calib’s accuracy and generalization, with DF-Calib achieving a mean translation error of 0.635cm and rotation error of 0.045° on the KITTI dataset.

I. INTRODUCTION

In modern robotic systems, such as autonomous driving, LiDAR and cameras are widely configured for their complementary capabilities. LiDAR provides high-precision 3D spatial measurement, while the camera captures detailed texture information. The fusion of the LiDAR point cloud and camera image is essential for advancing pivotal robotic technologies, *e.g.*, SLAM [1], [2] and object detection [3], [4], ultimately improving perception accuracy and robustness. A fundamental prerequisite in this process is precise extrinsic calibration, which ensures accurate spatial alignment of heterogeneous sensor data. General calibration methods [5], [6] typically rely on handcrafted targets, such as checkerboards. However, in real-world scenarios, mechanical vibrations and operational disturbances cause gradual deviation in extrinsic parameters, necessitating frequent recalibration. The reliance on specific targets makes target-based calibration cumbersome and impractical in dynamic environments. Therefore, developing online targetless calibration methods is crucial for enhancing adaptability and usability in real-world applications.

However, compared to offline target-based methods, online targetless calibration relies on natural environmental features for registration due to the absence of predefined calibration

targets. This exacerbates the challenge of bridging the significant modality gap between LiDAR point clouds and camera images, making it more difficult to achieve accurate extrinsic parameter estimation. Traditional online targetless methods [7], [8], [9] optimize extrinsic parameters by leveraging features such as edges, lane markings, and motion trajectories. However, their performance is constrained by the availability and consistency of these features, which may be sparse or unreliable in natural fields. As a result, these approaches become less effective in scenarios where preset cues are either insufficient or exhibit high variability.

To address this challenge, deep learning techniques have been introduced to reduce reliance on predefined targets and idealized conditions. Current learning-based methods [10], [11] typically extract features separately from the sparse depth map projected from the LiDAR point cloud and the camera image. Various approaches [12], [13] adopt an end-to-end framework, directly regressing extrinsic parameters with high accuracy but relying on specific camera configurations, limiting generalizability. In contrast, matching-based methods [14], [15] establish 2D-3D correspondences, decoupling extrinsic estimation from camera parameters and enhancing generalization. However, inherent modality differences lead to feature distribution discrepancies, making both paradigms struggle with consistent feature extraction and robust cross-modal alignment, ultimately compromising calibration accuracy. Furthermore, they fail to prioritize salient regions, such as edges or other structural areas, within the LiDAR and camera data, weakening critical feature influence and further degrading calibration accuracy. Recently, CalibDepth [16] reduces the modality gap by matching the sparse LiDAR-projected depth map with the camera estimated dense depth map. However, the LiDAR sparse depth map lacks the detailed geometric structures (*e.g.*, edges and surfaces) that are present in the camera dense depth map, leading to registration challenges that ultimately compromise calibration accuracy.

In this paper, we propose DF-Calib, a matching-based targetless LiDAR-camera calibration method designed to address the aforementioned problems via depth flow. We employ monocular geometry estimation to generate a dense depth map from the camera image and complete the sparse LiDAR-projected depth map into a dense representation, leveraging a shared feature encoder to extract consistent depth-to-depth features. Additionally, we introduce a reliability map to guide the model prioritizing features extracted from valid pixels, thus minimizing the impact of noise introduced during depth completion. Subsequently, we estimate a depth flow that incorporates 2D-3D correspondences between

Shu Han, Ji Wu, Ximeng Cai are with the School of Computer Science, Xubo Zhu, Wen Yang and Huai Yu are with the School of Electronic Information, Gui-Song Xia is with the School of Artificial Intelligence. All authors are with Wuhan University, Wuhan, China 430072. E-mail: {hanshu, zhuxubo, ji.wu, ximengcai, yangwen, yuhuai, guisong.xia}@whu.edu.cn

the camera and LiDAR data, followed by a PnP solver to calculate the extrinsic parameter. To further improve the accuracy of the depth flow, we propose the perceptually weighted sparse flow (PWSF) loss, which encourages the model to focus on pixels within the salient regions of the depth map. Our main contributions are listed as follows:

- We propose DF-Calib, a targetless LiDAR-camera calibration method that transforms the calibration task into an intra-modality depth flow estimation problem, achieving high calibration accuracy while improving generalization.
- We convert the camera image into a dense depth map and complete the sparse LiDAR depth map, employing a shared feature encoder to extract consistent depth-to-depth features, which effectively bridges the cross-modal gap and enhances calibration accuracy.
- We introduce a reliability map to prioritize features from valid pixels and propose a perceptually weighted sparse flow loss to focus on salient regions of the depth maps, enhancing depth flow and calibration accuracy.
- Our experimental results across multiple datasets, including KITTI Odometry, KITTI Raw, and KITTI-360, demonstrate that DF-Calib achieves accurate extrinsic calibration results and exhibits reliable generalization ability.

II. RELATED WORK

LiDAR-camera calibration can be broadly classified into target-based and targetless methods. While learning-based approaches are gaining prominence for their calibration accuracy and attracting considerable attention, we consider them a distinct category for further discussion.

A. Target-based Methods

Target-based LiDAR-camera calibration relies on calibration targets detectable in both modalities to establish accurate 2D-3D correspondences. Early methods [5], [6], [17] were inspired by camera intrinsic calibration using chessboard patterns. Over time, various calibration targets, such as plane boards with holes [18], triangles [19], polygons [20], spheres [21], and ArUco [22], have been developed to enhance feature extraction accuracy. While these methods improve calibration precision, the complex target designs increase production difficulty. Despite the high precision achievable, the reliance on targets introduces limitations related to accessibility and automation, making it unsuitable for online calibration.

B. Targetless Methods

Targetless methods eliminate the need for calibration targets by leveraging common features and generally establishing correspondences directly from natural scene structures. Frequently used features include edges [7] and lane markings [8], with extrinsic parameters optimized to maximize feature consistency.

To avoid relying on predefined features, Nagy *et al.* [23] recover 3D geometry using Structure-from-Motion (SfM)

and jointly optimize the extrinsic during the reconstruction process. Mutual information techniques [24], [25] align projected depth or intensity maps with camera images, optimizing the extrinsic by maximizing mutual information. Taylor *et al.* [9] employ motion-based approaches by matching trajectories but require diverse motion data for accurate optimization.

In summary, targetless methods use a range of features and metrics to formulate an optimization problem for the extrinsic. However, their effectiveness is highly dependent on initial conditions, assumption validity, and scene suitability.

C. Learning-based Methods

Learning-based methods leverage neural networks to autonomously extract features, eliminating the need for manually designed features and enabling more flexible calibration. These methods can be categorized into two types: regression-based and matching-based.

Regression-based methods employ an end-to-end approach where the network directly regresses extrinsic parameters. RegNet [10] pioneers this framework, defining a pipeline of feature extraction, matching, and global regression. CalibNet [11] further introduces geometric constraints to improve consistency. CalibRCNN [26] and CALNet [27] refine these techniques by incorporating temporal losses for improved stability. CalibDepth [16] enhances feature matching between the sparse LiDAR-projected depth map and the estimated dense depth map but struggles to align complex geometric structures (*e.g.*, lines and surfaces), reducing calibration accuracy. Despite their effectiveness, regression-based methods strongly depend on camera configurations, requiring retraining or fine-tuning for new sensor setups.

Matching-based methods, in contrast, decouple feature matching from pose estimation, establishing 2D-3D correspondences and formulating calibration as a PnP problem. This improves generalization across different camera configurations. CFNet [14] introduces calibration flow, leveraging the EPnP algorithm [28], while DXQ-Net [15] integrates a differentiable pose estimation module with uncertainty filtering. However, both regression-based and matching-based approaches face challenges in handling cross-modal inconsistencies, particularly in extracting consistent features, ultimately restricting calibration accuracy. Additionally, they generally overlook salient regions in the LiDAR and camera data, diminishing the impact of critical features and further degrading calibration performance.

Unlike existing methods, our approach converts both camera images and LiDAR point clouds into dense depth maps, from which we extract consistent depth-to-depth features. By estimating the depth flow between these maps, we establish 2D-3D correspondences and solve for extrinsic parameters via a PnP solver, effectively addressing the cross-modal challenge. Additionally, we employ PWSF loss to emphasize salient regions in the depth map, enhancing depth flow accuracy and calibration precision.

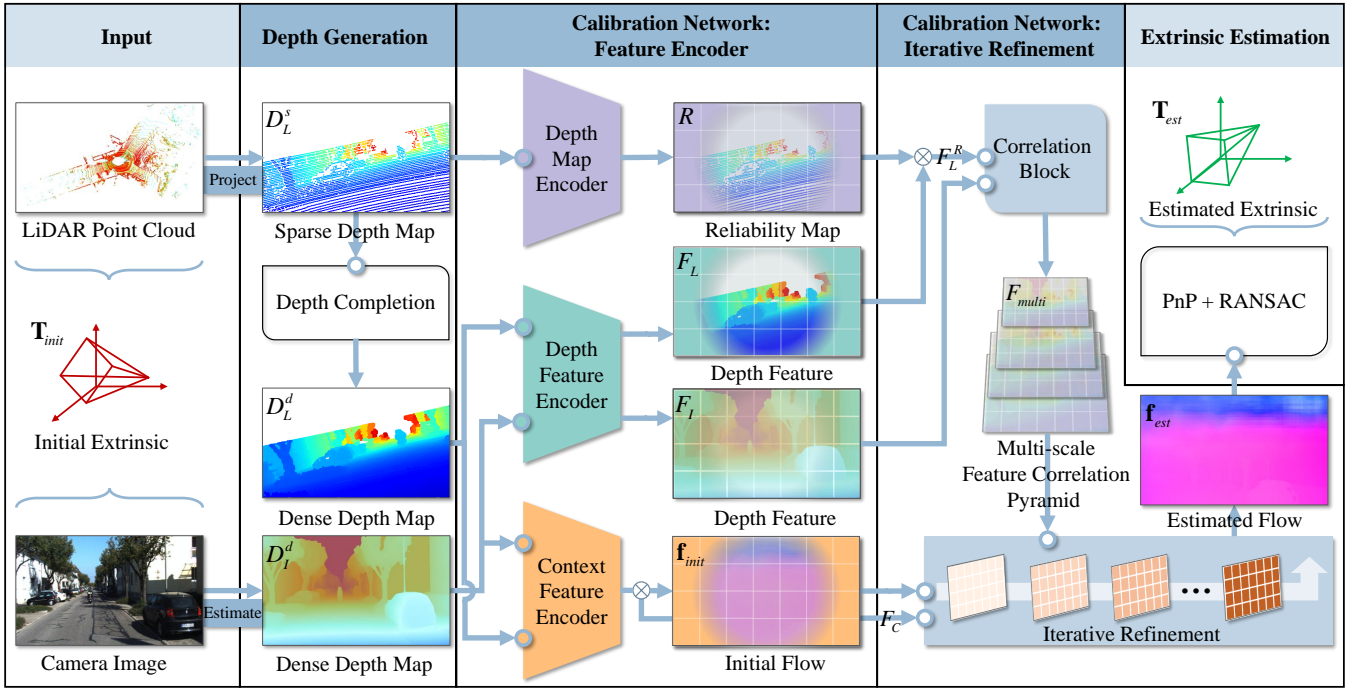


Fig. 1: Our proposed method first employs MOGE to estimate the dense depth map D_I^d from the camera image. Simultaneously, the LiDAR point cloud is projected onto the image plane, generating a sparse depth map D_L^s , further densifying into D_L^d . These three depth maps are input into the network to estimate a depth flow encapsulating the 2D-3D correspondences between the camera and LiDAR data. Ultimately, a 6-DoF transformation \mathbf{T}_{est} is computed via PnP with RANSAC.

III. PROPOSED METHOD

The inputs of the proposed method are a camera image and a LiDAR point cloud. The camera image is processed by MoGe [29] to estimate a dense depth map, while the LiDAR point cloud is projected into a sparse depth map and subsequently completed to a dense one. These three depth maps are fed into the network, which estimates a depth flow representing the 2D-3D correspondences between the camera and LiDAR data. Finally, the extrinsic parameter is estimated by the PnP solver. An overview of our method is shown in Fig. 1.

A. Problem Formulation

Given a misaligned camera image $I \in \mathbb{R}^{3 \times W \times H}$ from the camera and LiDAR point cloud $P_L \in \mathbb{R}^{3 \times N}$, the extrinsic calibration aim to estimate a 6-DoF extrinsic parameter $\mathbf{T}_{est} = [\mathbf{R}_{est}, \mathbf{t}_{est}] \in SE(3)$ that adjusts the initial extrinsic parameter $\mathbf{T}_{init} \in SE(3)$ for accurate sensor alignment. Here, W and H represent the image width and height, respectively. $\mathbf{R}_{est} \in SO(3)$ denotes the rotation matrix, and $\mathbf{t}_{est} \in \mathbb{R}^{3 \times 1}$ represents the translation vector. For matching-based methods, the 2D-3D correspondences between image pixels and LiDAR points are first established. The extrinsic parameter is then estimated via the PnP solver, with RANSAC to prune outliers and enhance robustness.

B. Depth Generation

The main challenge in LiDAR-camera extrinsic calibration lies in cross-modal data matching due to structure and information density differences between point clouds and images. To address this, we propose a novel method that transforms both modalities into dense depth maps, aligning

their structure and information density for effective matching. First, we employ MoGe [29] to estimate the dense depth map $D_I^d \in \mathbb{R}^{1 \times W \times H}$ from a camera image. Meanwhile, leveraging the camera's intrinsic parameter $\mathbf{K} \in \mathbb{R}^{3 \times 3}$ and initial extrinsic parameter $\mathbf{T}_{init} = [\mathbf{R}_{init}, \mathbf{t}_{init}]$, the LiDAR point cloud P_L is projected onto the pixel coordinate system, resulting in a sparse depth map $D_L^s \in \mathbb{R}^{1 \times W \times H}$. The projection process can be formulated as

$$d_i \begin{bmatrix} u_i \\ v_i \\ 1 \end{bmatrix} = \mathbf{K} \mathbf{T}_{init} \begin{bmatrix} x_i \\ y_i \\ z_i \\ 1 \end{bmatrix} = \mathbf{K} \begin{bmatrix} \mathbf{R}_{init} & \mathbf{t}_{init} \\ \mathbf{0} & 1 \end{bmatrix} \begin{bmatrix} x_i \\ y_i \\ z_i \\ 1 \end{bmatrix}, \quad (1)$$

where d_i represents the depth of each pixel, and $[x_i, y_i, z_i, 1]^T$ is the homogeneous coordinate of the 3D point, while $[u_i, v_i, 1]^T$ is the corresponding pixel's homogeneous coordinate in 2D. However, due to the inherent sparsity of LiDAR data, D_L^s contains only a limited number of valid pixels, leading to a significant information density disparity between D_L^s and D_I^d , which adversely affects subsequent depth flow estimation. To mitigate this issue, we employ an efficient depth completion method [30] to transform D_L^s into a dense depth map $D_L^d \in \mathbb{R}^{1 \times W \times H}$. As shown in Fig. 2, this process ensures that both the LiDAR point cloud and the camera image are effectively converted into dense depth maps, facilitating the subsequent depth flow estimation.

Inspired by the concept of optical flow estimation, we introduce depth flow $\mathbf{f} \in \mathbb{R}^{2 \times W \times H}$ as a pixel-wise displacement field between two depth maps for LiDAR-camera extrinsic calibration, capturing both horizontal and vertical shifts. The depth flow represents dense pixel correspondences between two depth maps while inherently establishes 2D-3D

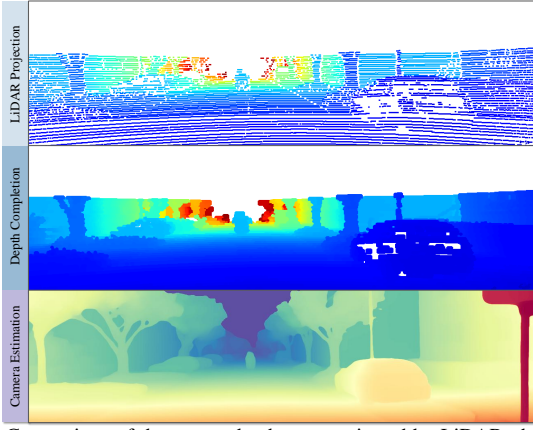


Fig. 2: Comparison of the sparse depth map projected by LiDAR, the dense depth map after depth completion, and the dense depth map estimated from the camera image. After completion, the depth maps generated by the LiDAR and the camera exhibit similar textures.

correspondences between the camera and the LiDAR data, which are subsequently used for extrinsic estimation.

To supervise the depth flow, we calculate the ground truth depth flow \mathbf{f}_{gt} based on the known discrepancy between the initial extrinsic parameter \mathbf{T}_{init} and the ground truth \mathbf{T}_{gt} . Given this, the pixel location $p_i = [u_i, v_i]^T \in \mathbb{R}^2$ in D_L^s deviates from its ground truth position $p_i^{gt} = [u_i^{gt}, v_i^{gt}]^T \in \mathbb{R}^2$. The ground truth depth flow \mathbf{f}_{gt} , which captures this displacement, is computed as

$$\mathbf{f}_{gt} = p_i^{gt} - p_i. \quad (2)$$

Here, \mathbf{f}_{gt} is further utilized for loss computation to enhance the calibration accuracy.

C. Calibration Network

Our network architecture is inspired by SEA-RAFT [31] and integrates LiDAR-projected and camera-estimated depth information to implement depth flow estimation.

1) *Feature Encoder*: As introduced in sect. III-B, we complete D_L^s to obtain D_L^d , which enhances the feature similarity between LiDAR and the camera depth maps. While D_L^s contains sparse, discontinuous data with limited point features, D_L^d incorporates more expressive line and surface features, making it texturally closer to D_I^d , as shown in Fig. 2. As a result, we can employ a shared depth feature encoder for both depth map D_L^d and D_I^d after they are normalized to the range $[-1, 1]$, reducing network complexity and facilitating the extraction of consistent depth-to-depth features, thereby enhancing calibration performance. Additionally, D_L^d and D_I^d are fed into a single context feature encoder to extract context information C from both LiDAR and camera data, which is subsequently decomposed into context features F_C and the initial depth flow \mathbf{f}_{init} .

However, depth completion introduces noise and blur effects, which may lead to the extraction of erroneous features, potentially undermining the accuracy of the extrinsic calibration. To address this issue, we utilize a depth map encoder to generate a reliability map R from D_L^s , guiding the model to prioritize features extracted from valid pixels. In the subsequent stage, R is used to enhance the accuracy of feature correlation.

2) *Iterative Refinement*: Based on the features extracted in the previous stage, we first apply element-wise multiplication between the features F_L extracted from D_L^d and the reliability map R to obtain the refined features F_L^R . Subsequently, following SEA-RAFT [31], we construct a multi-scale feature correlation pyramid F_{multi} between the depth features F_I extracted from D_I^d and F_L^R by computing the dot product between corresponding pixel pairs at each scale. The refinement block takes context features F_C , multi-scale features F_{multi} , and the depth flow \mathbf{f} as inputs, where \mathbf{f} is initially set to the initial depth flow \mathbf{f}_{init} . It then iteratively updates \mathbf{f} through a recurrent refinement process, progressively enhancing the accuracy of the estimated depth flow. The final refined depth flow, representing the 2D-3D correspondences, is subsequently processed by PnP with RANSAC to compute the extrinsic parameter \mathbf{T}_{est} .

D. Loss Function

Since the ground truth depth flow \mathbf{f}_{gt} is derived from the projection of the sparse LiDAR point cloud, it only contains valid information at a sparse set of pixels. Directly applying a standard \mathcal{L}_1 loss to all pixels would allow these invalid pixels to negatively impact the estimation performance of the final depth flow. To mitigate this issue, we introduce a valid mask $v(p)$ that filters out invalid pixels, defined as follows:

$$v(p) = \begin{cases} 1, & \mathbf{f}_{gt}(p) \neq 0, \\ 0, & \text{otherwise.} \end{cases} \quad (3)$$

During depth flow estimation, regions characterized by significant depth variations generally correspond to object boundaries or other critical structural features, which are paramount for accurate flow estimation. Conventional \mathcal{L}_1 loss function treats all pixels equally, which leads to sub-optimal learning performance, particularly in areas with sharp depth discontinuities, where flow estimation errors are more perceptible and visually significant. Emphasizing these regions helps prioritize critical features, thereby enhancing depth flow estimation accuracy.

Building upon this principle, we propose the perceptually weighted sparse flow (PWSF) loss, which adaptively emphasizes depth flow errors in these critical regions while maintaining overall sparsity within the flow field. Specifically, the PWSF loss is formulated as follows:

$$\mathcal{L}_{PWSF} = \frac{1}{S} \sum_p \left(\alpha_i(p) \alpha_j(p) \|\mathbf{f}_{gt}(p) - \mathbf{f}_{pre}(p)\|_1 + (1 - \alpha_i(p)) \|\mathbf{f}_{gt}(p) - \mathbf{f}_{pre}(p)\|_1 \right) v(p), \quad (4)$$

where $S = \sum_p v(p)$ is the sum of the valid pixels. $\alpha \in \mathbb{R}^{2 \times H \times W}$ represents the model-predicted importance map, $\alpha_i \in \mathbb{R}^{1 \times H \times W}$ representing the likelihood of each pixel belonging to the salient regions, indicating its importance, and $\alpha_j \in \mathbb{R}^{1 \times H \times W}$ controlling the weighting of the corresponding loss term. Based on the predicted importance of each pixel, the importance map adjusts the weight of the loss components. For pixels with higher predicted importance, indicating they are likely to lie within salient regions, the

TABLE I: Different environmental setups

Name	Dataset	Perturbation	Training	Test
Exp1	KITTI Odometry	5°, 0.10m	01-21	00
Exp2	KITTI Odometry	10°, 0.25m	01-21	00
Exp3	KITTI Raw	10°, 0.25m	2011-9-26	2011-9-30
Exp4	KITTI-360	10°, 0.25m	/	Test-SLAM

weighted \mathcal{L}_1 loss is emphasized. In contrast, the standard \mathcal{L}_1 loss dominates. This strategy ensures the overall sparsity of the flow field while effectively prioritizing accuracy in regions with critical structural details.

Finally, the total loss is computed as an exponentially weighted sum of the PWSF loss across all iterations:

$$\mathcal{L}_{total} = \sum_{i=1}^N \gamma^{N-i} \mathcal{L}_{PWSF}^i, \quad (5)$$

where N denotes the total number of iterations, and $\gamma < 1$ is an exponential decay factor that reduces the influences of later iterations. The term \mathcal{L}_{PWSF}^i is the PWSF loss at the i -th iteration. This weighted summation ensures that earlier iterations contribute more significantly to the optimization process, promoting a more stable and progressive refinement of the depth flow.

IV. EXPERIMENTS

In this section, we conduct comprehensive experiments on the KITTI Raw [34], KITTI Odometry [34], and KITTI-360 [35] datasets to compare DF-Calib with the state-of-the-art approaches, validating its effectiveness and generalization capability.

A. Dataset Preparation

Following existing methods [12], [16], a random perturbation $\Delta\mathbf{T}$ within a certain range is added to the ground truth extrinsic parameter \mathbf{T}_{gt} to obtain the initial extrinsic parameter $\mathbf{T}_{init} = \Delta\mathbf{T}^{-1} \times \mathbf{T}_{gt}$. The LiDAR point cloud is transformed using \mathbf{T}_{init} to ensure that the updated ground truth extrinsic parameter \mathbf{T}'_{gt} is $\Delta\mathbf{T}$.

Since there is no standardized experimental setup for LiDAR-camera extrinsic calibration, different experimental configurations are set for comparison, as shown in Table I.

1) : Exp1 follows the configuration of DXQ-Net [15], where sequences 01 to 21 of the KITTI Odometry dataset are used for training and validation, and sequence 00 is used for testing, with the initial perturbation of (5°, 0.10m).

2) : Exp2 follows the setup of CalibFormer [12], where sequences 01 to 21 of the KITTI Odometry dataset are used for training and validation, while sequence 00 is used for testing. The initial perturbation is set to (10°, 0.25m).

3) : Exp3 is based on CalibDepth [16] and CalibLG [13], where 24,000 pairs from sequence 2011-9-26 of the KITTI Raw dataset are used for training and validation, and sequence 2011-9-30 is used for testing. The initial perturbation remained (10°, 0.25m).

4) : Exp4 is designed to evaluate the generalization ability of the proposed method. The model trained using the Exp3 setup is directly tested on the Test-SLAM subset of the KITTI-360 dataset, with the same initial perturbation as Exp3 (10°, 0.25m).

B. Experimental Settings

1) *Implementation Details*: All images are cropped to a resolution of 960×320 , with the camera intrinsic parameter adjusted accordingly for LiDAR point cloud projection. The AdamW optimizer is used with a weight decay of 1×10^{-5} and an initial learning rate of 1×10^{-4} . The OneCycleLR scheduler is employed for learning rate adjustment. The model is trained for 100 epochs with a batch size of 6, and the number of iterative refinement is set to 4 during training. All the experiments are conducted on a single NVIDIA RTX 4090 GPU.

2) *Evaluation Metrics*: The evaluation of LiDAR-camera extrinsic calibration methods is based on the rotation and translation errors between the estimated extrinsic parameter \mathbf{T}_{est} and the ground truth \mathbf{T}'_{gt} . The rotation error is measured using Euler angles, where the mean absolute errors are computed separately for roll, pitch, and yaw. The translation error is assessed by calculating the mean absolute distance error along the x, y, and z directions.

C. Experimental Results

In this section, we analyze the quantitative and qualitative results of DF-Calib compared to other methods. Additionally, we examine its runtime performance.

Quantitative Results. As shown in Table II, DF-Calib is evaluated against seven state-of-the-art approaches across various initial deviations and datasets, including NetCalib [32], DXQ-Net [15], CALNet [27], PSNet [33], CalibFormer [12], CalibDepth [16] and CalibLG [13].

1) *Exp1*: DF-Calib achieves a mean translation error of 0.635cm and a mean rotation error of 0.045°. When compared to DXQ-Net, a matching-based method without region prioritization, DF-Calib maintains comparable rotation error while greatly reducing the translation error by 18.0%. This improvement stems from the PWSF loss, which prioritizes salient regions in LiDAR and camera data, enhancing depth flow estimation and calibration precision.

2) *Exp2&3*: DF-Calib achieves a mean translation error of 1.065cm and a mean rotation error of 0.058° in Exp2, surpassing CalibFormer, which regresses the extrinsic from a camera image and a sparse LiDAR depth map, by 10.4% and 58.9%, respectively. In Exp3, it attains a mean translation error of 2.271cm and a mean rotation error of 0.091°, outperforming CalibLG, another regression-based method using the same inputs, by 40.4% and 62.1%. These improvements arise from DF-Calib’s reformulation of the calibration task as an intra-modality depth flow estimation problem, enhancing feature consistency and significantly boosting the accuracy of both translation and rotation estimation.

3) *Exp4*: DF-Calib achieves a mean translation error of 5.598cm and a mean rotation error of 0.326° on the KITTI-360 dataset without being trained on it, outperforming CalibDepth, the only open-source method among the baselines, by 70.2% and 86.5%, respectively. This strong generalization ability stems from DF-Calib being a matching-based method, which decouples calibration from camera intrinsics and enhances adaptability to diverse camera configurations.

TABLE II: Comparison results on different environmental setups

Dataset	Method	Translation (cm) ↓				Rotation (°) ↓			
		Mean	X	Y	Z	Mean	Roll	Pitch	Yaw
Exp1	NetCalib[32]	1.291	1.618	0.917	1.337	0.125	0.083	0.189	0.103
	DXQ-Net [15]	0.774	0.754	0.476	1.091	0.042	0.049	0.046	0.032
	DF-Calib	0.635	0.698	0.569	0.638	0.045	0.046	0.045	0.045
Exp2	CALNet[27]	3.03	3.65	1.63	3.80	0.20	0.10	0.38	0.12
	PSNet[33]	3.1	3.8	2.8	2.6	0.15	0.06	0.26	0.12
	CalibFormer[12]	1.188	1.101	0.902	1.561	0.141	0.076	0.259	0.087
	DF-Calib	1.065	1.258	1.018	0.917	0.058	0.063	0.056	0.056
Exp3	CalibDepth[16]	4.75	6.66	1.12	6.48	0.348	0.180	0.862	0.181
	NetCalib[32]	4.38	6.55	3.10	3.50	0.378	0.200	0.561	0.372
	CalibLG[13]	3.81	3.24	3.93	4.25	0.240	0.086	0.361	0.280
	DF-Calib	2.271	3.173	2.211	1.429	0.091	0.110	0.071	0.091
Exp4	CalibDepth[16]	18.796	26.987	12.208	17.193	2.418	3.833	0.752	2.650
	DF-Calib	5.598	5.697	4.553	6.544	0.326	0.388	0.325	0.266

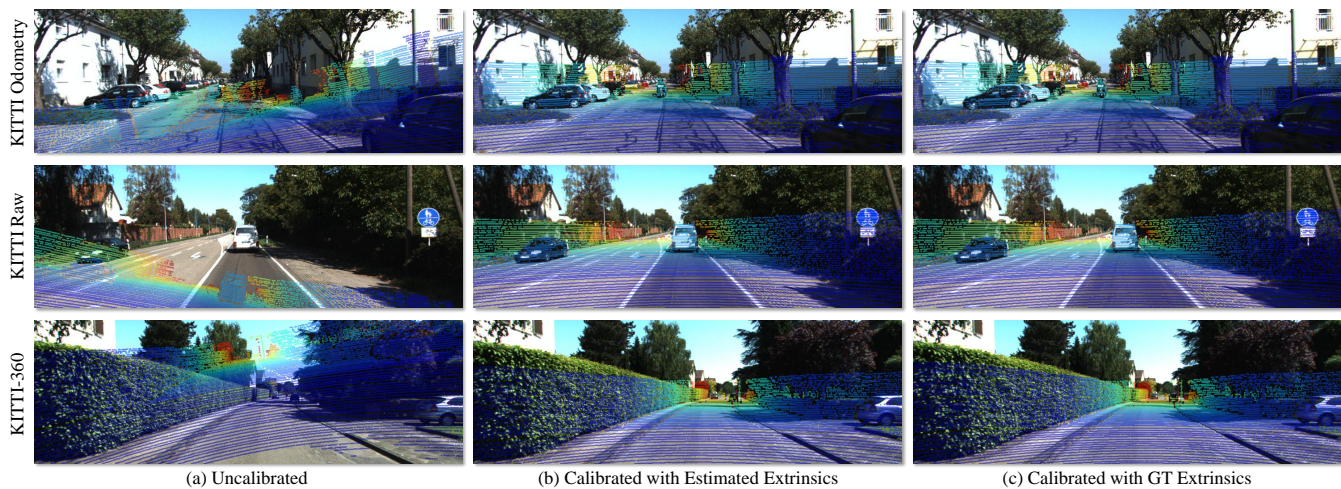


Fig. 3: Overlay of RGB images with LiDAR projections using uncalibrated, calibrated, and GT extrinsics, respectively, across KITTI Odometry, KITTI Raw and KITTI-360 datasets.

TABLE III: Ablation studies on different components in DF-Calib

Method	KITTI Odometry		KITTI Raw	
	Trans. (cm) ↓	Rot. (°) ↓	Trans. (cm) ↓	Rot. (°) ↓
w/o D	3.673	1.563	6.842	3.122
w/o S	1.154	0.067	2.452	0.102
w/o D, S	1.343	0.072	2.52	0.121
w/o R	1.211	0.066	2.581	0.103
w/o P	2.124	0.102	3.989	0.198
w/ all	1.065	0.058	2.271	0.091

D, S, R, and P represent Completed Dense Depth Map, Shared Feature Encoder, Reliability Map, and PWSF Loss, respectively.

Qualitative Results. As shown in Fig. 3, DF-Calib’s estimated extrinsics closely align with the ground truth across diverse scenarios and initial deviation conditions, highlighting its robustness to a wide range of initial errors and effectiveness in handling complex environments.

Runtime Analysis. We optimize MoGe by removing unnecessary operations, and reducing depth estimation to 38 ms. In parallel, LiDAR projection and depth completion take 12 ms. Then depth flow estimation takes 31 ms, and the PnP solver 25 ms, totaling about 95 ms. This enables calibration at about 11 Hz, acceptable for real-time applications.

D. Ablation Study

We conduct ablation experiments on the KITTI Odometry and KITTI Raw datasets under an initial perturbation of $(10^\circ, 0.25\text{m})$ to evaluate the effectiveness of our proposed components, using mean absolute translation error and mean absolute rotation error as evaluation metrics. The results are shown in Table III.

Without completing the sparse LiDAR depth map and directly using it with the image-estimated dense depth map D_I^d via a shared feature encoder, the error approximately tripled, demonstrating that depth completion reduces the information density gap and enhances feature consistency. When processing D_L^d and D_I^d with separate encoders instead of a shared one, the error increased by about 10%, and model parameters grew from 19M to 28M, highlighting the shared encoder’s efficiency in feature extraction and network complexity reduction. Removing both depth completion and the shared encoder led to an approximate 25% increase in error and a 47% rise in model parameters, reinforcing their importance.

Removing the constraint of the Reliability Map on dense depth features resulted in an error increase of around 15% on both datasets, indicating its role in suppressing noise

introduced by depth completion. Replacing the PWSF loss with standard \mathcal{L}_1 loss approximately doubles the error, demonstrating that PWSF loss effectively filters out invalid points and prioritizes salient regions, improving depth flow estimation and overall accuracy.

V. CONCLUSION

In this paper, we propose DF-Calib, a targetless LiDAR-camera calibration method that reformulates the task as an intra-modality depth flow estimation problem. We unify LiDAR and camera data into a dense depth representation to bridge the modality gap. This facilitates more effective feature matching via a shared feature encoder and utilizes a reliability map to prioritize valid points, thereby enhancing calibration accuracy. Additionally, we introduce a perceptually-weighted sparse flow loss, which improves calibration precision by emphasizing salient regions. Experimental results on multiple datasets demonstrate the effectiveness of DF-Calib, achieving accurate extrinsic calibration and robust generalization across diverse setups. In the future, we will explore the use of depth flow for calibrating other heterogeneous sensors to adapt to diverse robotic platforms.

REFERENCES

- [1] C. Zheng, Q. Zhu, W. Xu, X. Liu, Q. Guo, and F. Zhang, "FAST-LIVO: Fast and tightly-coupled sparse-direct LiDAR-inertial-visual odometry," in *Proc. IEEE/RSJ Int. Conf. Intell. Robots Syst.*, 2022, pp. 4003–4009.
- [2] J. Lin and F. Zhang, "R³LIVE: A robust, real-time, RGB-colored, LiDAR-inertial-visual tightly-coupled state estimation and mapping package," in *Proc. Int. Conf. Robot. Automat.*, 2022, pp. 10672–10678.
- [3] Y. Li, A. W. Yu, T. Meng, B. Caine, J. Ngiam, D. Peng, J. Shen, Y. Lu, D. Zhou, Q. V. Le, *et al.*, "DeepFusion: LiDAR-camera deep fusion for multi-modal 3D object detection," in *Proc. IEEE/CVF Conf. Comput. Vis. Pattern Recognit.*, 2022, pp. 17182–17191.
- [4] X. Guo, S. Shi, X. Wang, and H. Li, "LIGA-Stereo: Learning LiDAR geometry aware representations for stereo-based 3D detector," in *Proc. IEEE/CVF Int. Conf. Comput. Vis.*, 2021, pp. 3153–3163.
- [5] Q. Zhang and R. Pless, "Extrinsic calibration of a camera and laser range finder (improves camera calibration)," in *Proc. IEEE/RSJ Int. Conf. Intell. Robots Syst.*, 2004, pp. 2301–2306.
- [6] R. Unnikrishnan and M. Hebert, "Fast extrinsic calibration of a laser rangefinder to a camera," *Robotics Institute, Pittsburgh, PA, Tech. Rep. CMU-RI-TR-05-09*, 2005.
- [7] J. Castorena, U. S. Kamilov, and P. T. Boufounos, "Autocalibration of LiDAR and optical cameras via edge alignment," in *Proc. IEEE Int. Conf. Acoust., Speech, Signal Process.*, 2016, pp. 2862–2866.
- [8] T. Ma, Z. Liu, G. Yan, and Y. Li, "CRLF: Automatic calibration and refinement based on line feature for LiDAR and camera in road scenes," *arXiv preprint arXiv:2103.04558*, 2021.
- [9] Z. Taylor and J. Nieto, "Motion-based calibration of multimodal sensor extrinsics and timing offset estimation," *IEEE Trans. Robot.*, vol. 32, no. 5, pp. 1215–1229, 2016.
- [10] N. Schneider, F. Piewak, C. Stiller, and U. Franke, "RegNet: Multimodal sensor registration using deep neural networks," in *Proc. IEEE Intell. Vehicles Symp.*, 2017, pp. 1803–1810.
- [11] G. Iyer, R. K. Ram, J. K. Murthy, and K. M. Krishna, "CalibNet: Geometrically supervised extrinsic calibration using 3D spatial transformer networks," in *Proc. IEEE/RSJ Int. Conf. Intell. Robots Syst.*, 2018, pp. 1110–1117.
- [12] Y. Xiao, Y. Li, C. Meng, X. Li, J. Ji, and Y. Zhang, "CalibFormer: A transformer-based automatic LiDAR-camera calibration network," in *Proc. Int. Conf. Robot. Automat.*, 2024, pp. 16714–16720.
- [13] S. Moon, S. Lee, D. He, and S.-E. Yoon, "LiDAR-camera online calibration by representing local feature and global spatial context," in *Proc. IEEE/RSJ Int. Conf. Intell. Robots Syst.*, 2024, pp. 9447–9454.
- [14] X. Lv, S. Wang, and D. Ye, "CFNet: LiDAR-camera registration using calibration flow network," *Sens.*, vol. 21, no. 23, p. 8112, 2021.
- [15] X. Jing, X. Ding, R. Xiong, H. Deng, and Y. Wang, "DXQ-Net: Differentiable LiDAR-camera extrinsic calibration using quality-aware flow," in *Proc. IEEE/RSJ Int. Conf. Intell. Robots Syst.*, 2022, pp. 6235–6241.
- [16] J. Zhu, J. Xue, and P. Zhang, "CalibDepth: Unifying depth map representation for iterative LiDAR-camera online calibration," in *Proc. Int. Conf. Robot. Automat.*, 2023, pp. 726–733.
- [17] B. Guan, J. Zhao, Z. Li, F. Sun, and F. Fraundorfer, "Relative pose estimation with a single affine correspondence," *IEEE Transactions on Cybernetics*, vol. 52, no. 10, pp. 10111–10122, 2022.
- [18] G. Yan, F. He, C. Shi, P. Wei, X. Cai, and Y. Li, "Joint camera intrinsic and LiDAR-camera extrinsic calibration," in *Proc. Int. Conf. Robot. Automat.*, 2023, pp. 11446–11452.
- [19] S. Debattisti, L. Mazzei, and M. Panciroli, "Automated extrinsic laser and camera inter-calibration using triangular targets," in *Proc. IEEE Intell. Vehicles Symp.*, 2013, pp. 696–701.
- [20] Q. Liao, Z. Chen, Y. Liu, Z. Wang, and M. Liu, "Extrinsic calibration of lidar and camera with polygon," in *Proc. IEEE Int. Conf. Robot. Biomim.*, 2018, pp. 200–205.
- [21] G. Zhang, K. Wu, J. Lin, T. Wang, and Y. Liu, "Automatic extrinsic parameter calibration for camera-LiDAR fusion using spherical target," *IEEE Robot. Automat. Lett.*, vol. 9, no. 6, pp. 5743–5750, 2024.
- [22] A. Dhall, K. Chelani, V. Radhakrishnan, and K. M. Krishna, "LiDAR-camera calibration using 3D-3D point correspondences," *arXiv preprint arXiv:1705.09785*, 2017.
- [23] B. Nagy, L. Kovács, and C. Benedek, "SFM and semantic information based online targetless camera-LiDAR self-calibration," in *Proc. IEEE Int. Conf. Image Process.*, 2019, pp. 1317–1321.
- [24] G. Pandey, J. McBride, S. Savarese, and R. Eustice, "Automatic targetless extrinsic calibration of a 3D LiDAR and camera by maximizing mutual information," in *Proc. AAAI Conf. Artif. Intell.*, vol. 26, no. 1, 2012, pp. 2053–2059.
- [25] B. Guan, J. Zhao, D. Barath, and F. Fraundorfer, "Minimal solvers for relative pose estimation of multi-camera systems using affine correspondences," *International Journal of Computer Vision*, vol. 131, no. 1, pp. 324–345, 2023.
- [26] J. Shi, Z. Zhu, J. Zhang, R. Liu, Z. Wang, S. Chen, and H. Liu, "CalibRCNN: Calibrating camera and LiDAR by recurrent convolutional neural network and geometric constraints," in *Proc. IEEE/RSJ Int. Conf. Intell. Robots Syst.*, 2020, pp. 10197–10202.
- [27] H. Shang and B.-J. Hu, "CALNet: LiDAR-camera online calibration with channel attention and liquid time-constant network," in *Proc. Int. Conf. Pattern Recognit.*, 2022, pp. 5147–5154.
- [28] V. Lepetit, F. Moreno-Noguer, and P. Fua, "EPnP: An accurate $O(n)$ solution to the PnP problem," *Int. J. Comput. Vision*, vol. 81, pp. 155–166, 2009.
- [29] R. Wang, S. Xu, C. Dai, J. Xiang, Y. Deng, X. Tong, and J. Yang, "MoGe: Unlocking accurate monocular geometry estimation for open-domain images with optimal training supervision," *arXiv preprint arXiv:2410.19115*, 2024.
- [30] J. Ku, A. Harakeh, and S. L. Waslander, "In defense of classical image processing: fast depth completion on the CPU," in *Proc. Conf. Comput. Robot. Vis.*, 2018, pp. 16–22.
- [31] Y. Wang, L. Lipson, and J. Deng, "SEA-RAFT: Simple, efficient, accurate RAFT for optical flow," in *Proc. Eur. Conf. Comput. Vis.*, 2024, pp. 36–54.
- [32] S. Wu, A. Hadachi, D. Vivet, and Y. Prabhakar, "NetCalib: A novel approach for LiDAR-camera auto-calibration based on deep learning," in *Proc. Int. Conf. Pattern Recognit.*, 2021, pp. 6648–6655.
- [33] Y. Wu, M. Zhu, and J. Liang, "PSNet: LiDAR and camera registration using parallel subnetworks," *IEEE Access*, vol. 10, pp. 70553–70561, 2022.
- [34] A. Geiger, P. Lenz, and R. Urtasun, "Are we ready for autonomous driving? the KITTI vision benchmark suite," in *Proc. IEEE/CVF Conf. Comput. Vis. Pattern Recognit.*, 2012, pp. 3354–3361.
- [35] Y. Liao, J. Xie, and A. Geiger, "KITTI-360: A novel dataset and benchmarks for urban scene understanding in 2D and 3D," *IEEE Trans. Pattern Anal. Mach. Intell.*, vol. 45, no. 3, pp. 3292–3310, 2022.